7

MAGNETOOPTICS OF GRANULAR MATERIALS AND NEW OPTICAL METHODS OF MAGNETIC NANOPARTICLES AND NANOSTRUCTURES IMAGING

V. I. Belotelov

Institute of General Physics, RAS, Moscow, Russia; and M. V. Lomonosov Moscow State University, Faculty of Physics, Physics of Oscillations Department, Moscow, Russia

P. Perlo

Fiat Research Center, Orbassano, Italy

A. K. Zvezdin

Institute of General Physics, RAS, Moscow, Russia; and Fiat Research Center, Orbassano, Italy

1. INTRODUCTION

Among different methods of investigation of magnetic objects, optical methods take leading positions because of their relative simplicity and self-descriptiveness. Magnetooptics of the uniform magnetic media and magnetic structures with the size greater than the wavelength of electromagnetic radia-

Metal-Polymer Nanocomposites, Edited by Luigi Nicolais and Gianfranco Carotenuto
ISBN 0-471-47131-3

tion has been studied in detail for the last several decades. Magnetooptical (MO) techniques of such objects allowed investigation of their magnetic structure both in statics and in dynamics. By means of these methods, images of the magnetization distribution can be obtained in polarization microscopy on the bases of the Faraday, Kerr, or Voigt effects.

At the same time, nowadays, there is great interest in the study of the magnetic properties of low-dimension systems, nanostructures, and granular materials. Magnetic nanostructures are viewed as a promising material for ultrahigh density (up to 1 Tbit/cm^2) data recording. Note that such a giant record density approaches the superparamagnetic limit (10 Tbit/cm^2) [1], which seems to be the ultimate value of the surface record density (today's value is 30 Gbit/cm^2 [2]). The typical size of a one-domain magnetic particle in structured nanomedia is estimated at 5–100 nm. MO investigations of nanostructures are also being conducted and yield fruit. Conventional methods like MO Faraday and Kerr observation along with new optical methods, such as scanning near-field optical microscopy and polarized microscopy, can give a great amount of information about these structures.

Usually, MO methods in their adaptation to the nanoscale world preserve simplicity in realization and cheapness. Optical imaging of magnetic structures is nondestructive, provides high sensitivity, and is not limited by protective nonmagnetic layers. Most importantly, magnetooptical imaging does not require magnetic probes, in contrast to magnetic force microscopy, and consequently does not influence the magnetic structure under investigation and allows measurements in applied magnetic field. Spatial resolution that can be achieved in MO imaging [in scanning near-field optical microscopy (SNOM)] is of the same order (10 nm) as the best resolution obtained by other (e.g., magnetic force microscopy) methods. At the same time some MO methods (e.g., MO Kerr magnetometry) also perform high temporal resolution.

Nevertheless, some difficulties in the experimental setup arise: organization of high precision sample positioning, smooth displacements, production of miniature probes, and so on. At the same time, new features of interaction between light and nanoscaled magnetic objects have not been fully studied, and theory techniques for nanoscale magnetooptics have been poorly developed. MO properties of nano-sized objects strongly depend on their transport properties (conductivity). They are also greatly influenced by quantum effects; consequently, dielectric tensor for bulk media is no longer appropriate for their description.

Taking, the aforesaid, into account, elaboration of consistent theory for the determination of transport and optical properties of magnetic nanostructures is quite urgent. Along with that, some improvements and innovations in experimental technique are also needed in this area.

Magnetooptics of granular materials and other nanoscaled magnetic objects is a thriving part of modern optics. At present it is only in the initial stages, and further investigation in this direction are to be performed.

In this chapter we give a brief outline of the conventional magnetooptics of granular materials, and then we discuss some theoretical and experimental aspects of MO observations of nanoscale magnetic structures.

2. OPTICS OF THE COMPOSITE MEDIA

In this section we shall consider propagation of the electromagnetic radiation through the media with inhomogeneities—that is, composite media. For example, it can be randomly spaced metallic particles embedded into dielectric polymer matrix. In general, when a wave propagates in the same medium, it does not resolve the individual particles, and the composite appears as a homogeneous material. Let us consider this question in more detail. When a heterogeneous material is probed by an electromagnetic wave, the resolution limit of the probing wave is set by $\lambda/2$. In addition, the Rayleigh scattering strength varies as λ^{-4}. It follows that in the so-called long wavelength limit the heterogeneous material would appear homogeneous to the probing wave, with the material properties characterized by effective parameters. In the long wavelength approximation it is possible to regard the material as being homogeneous and possessing an appropriate effective value of the permittivity, permeability, and conductivity. These effective parameters can be found in terms of the properties of the composite constituent phases by means of a homogenization procedure or an effective-medium theory. Since for the optical frequencies the range permeability constant is close to unity, we in what follows shall consider only dielectric constant [3].

Two main composite topologies should be marked out: cermet and aggregate (Figure 7.1) [4]. In the cermet topology, each inclusion is completely surrounded by host material; and for not very large filling factors of the metallic phase composite, it performs as a dielectric material. For the aggregate topology the metallic inclusions are allowed to touch, making the composite conductive. The transition between these two topologies happens when the filling factor reaches the percolation threshold f_{pc} at which the metallic network first becomes connected. In the vicinity of f_{pc}, the dielectric constant and therefore the optical properties exhibit dramatic changes. In general, the percolation threshold occurs at $0.2 < f_{pc} < 0.75$. Thus for cubic lattices the maximum possible f are 0.52, 0.68, and 0.74, for sc, bcc, and fcc lattices, respectively [5]. In Co–SiO_2 for instance, f_{pc} is about 0.55, while it equals to 0.25 for Co–Al_2O_3 [6].

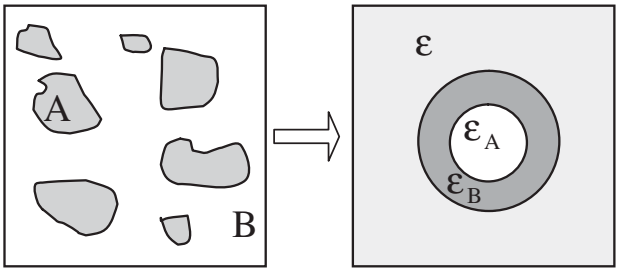

(a)

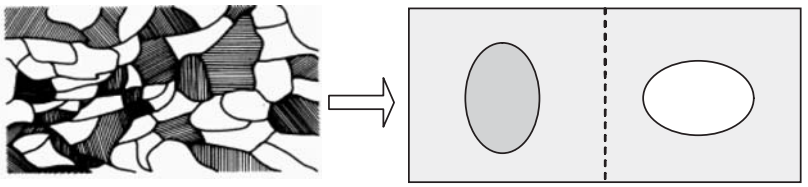

(b)

Figure 7.1. Effective medium theory approach for cermet (**a**) and aggregate (**b**) topologies.

In regular arrays the percolation transition is sharp, because all of the spheres approach contact at once. Practically no ordered structure of the inclusions can take place in the composite. That is why when f is not very small, disordered composites generally contain (a) local metallized regions (particle clusters) where the critical density has been reached and (b) other nonmetallized (dielectric) regions with lower local particle densities. With increasing volume filling factor f, the metallized clusters grow at the expense of the dielectric regions. Thus, in contrast with the behavior of regular arrays, the metallization transition in disordered composites occurs at different times in different regions of the sample. Nevertheless, at $f = f_{pc}$ the entire suspension becomes conductive.

There are a number of formulas for the determination of the effective dielectric constant: Maxwell Garnett (MG) formula, Bruggeman (BG) equation, Hanai–Bruggeman (HBG) formulas, empirical Lichtenecker mixture equations, and so on.

The empirical equations are obtained by the intuitive suggestions with the use of experimental data. Here we cite an instance of two Lichtenecker equations [7–9] for two-phase and multiphase composites:

$$|\varepsilon_{\text{eff}}| = (1-f)|\varepsilon_1| + f|\varepsilon_2|, \qquad \frac{\varepsilon_{\text{eff}}''}{\varepsilon_{\text{eff}}'} = \frac{\varepsilon_1''}{\varepsilon_1'} + \frac{\varepsilon_2''}{\varepsilon_2'}, \qquad \ln \varepsilon_{\text{eff}} = \sum_i f_i \ln \varepsilon_i$$

where f_i is the volume fraction of ith constituent, and ε_i' and ε_i'' are real and imaginary parts of the dielectric constant, respectively. For other empirical formulas, one can address the following references.

The MG, BG, and HBG formulas are based on the more comprehensive approaches, one of which is presented further.

2.1. Homogenization Technique, the Effective-Medium Formulas

The approach is based on considering the composite as made up of elementary structural units (ESU)—that is, in fact, the main principle of the effective-medium theory [4, 10, 11]. For example, in a composite with the cermet topology, the basic unit may be taken as a coated grain (Figure 7.1a). If the inclusions are allowed to touch—that is, if the aggregate topology is presented—then the two phases should be considered on an equal basis, and a grain of constituent A and a grain of constituent B are two basic units (Figure 7.1b). Once the ESU are chosen, the next step is the embedding of each individual unit in a homogeneous effective medium characterized by a yet-undetermined effective dielectric constant ε_{eff} or effective conductivity σ_{eff}.

The basic definition of an effective medium is that the ESU, when embedded in the effective medium, should not be detectable in an experiment using electromagnetic measurement. In other words, the extinction of the ESU should be the same as if it were replaced with a material characterized by ε_{eff}. This criterion makes it fruitful to use a recently derived [12] "optical theorem" for absorbing media; it relates the extinction of the spherical cell compared to that of the surrounding medium with the scattering amplitude in the direction of the impinging beam $S(0)$ (forward scattering amplitude) by

$$C_{\text{ext}} = 4\pi \operatorname{Re}\left[S(0)/k^2\right]$$

where k is the wave vector of the light in the effective medium. From the definition of an effective medium, it follows that $C_{\text{ext}} = 0$, that is $S(0) = 0$, which expresses the fundamental property of an effective medium. Consequently, the effective-medium general condition is then [13]

$$\sum_i f_i S_i(0) = 0 \tag{1}$$

where f_i is the volume fraction of the ith unit. Since $S_i(0)$ is an implicit function of ε_{eff}, equation (1) represents a condition for its determination.

If ESU is a coated sphere (Figure 7.1a), then the Lorenz–Mie [14] theory gives $S(0)$ as

$$S(0) = i(kb)^3 \frac{(\varepsilon_B - \varepsilon)(\varepsilon_B - \varepsilon) + f_A(2\varepsilon_B + \varepsilon)(\varepsilon_A - \varepsilon_B)}{(\varepsilon_B + 2\varepsilon)(\varepsilon_A + 2\varepsilon_B) + f_A(2\varepsilon_B - 2\varepsilon)(\varepsilon_A - \varepsilon_B)} + O\left((kb)^5\right)$$

The filling factor is

$$f = \frac{a^3}{b^3}$$

where $a(b)$ is the radius of the inner (outer) sphere in Figure 7.1a. This yields the Maxwell Garnett formula

$$\varepsilon_{eff} = \varepsilon_B \frac{\varepsilon_A(1+2f) + 2\varepsilon_B(1-f)}{\varepsilon_A(1-f) + \varepsilon_B(2+f)} \tag{2}$$

which is often written in a different form:

$$\frac{\varepsilon_{\text{eff}} - \varepsilon_B}{\varepsilon_{\text{eff}} + 2\varepsilon_B} = f \frac{\varepsilon_A - \varepsilon_B}{\varepsilon_A + 2\varepsilon_B}$$

The MG approach is applicable for so-called cermet topology [15, 16]. This formula has been accepted as satisfactory when the exact interparticle interactions are not important—for example, in the case of dilute dispersions or components of low polarizabilities.

For small volume fractions, by expanding equation (2) to the first order in the volume fraction, one can find the absorption coefficient of the composite α that is related to the imaginary part of ε_{eff}:

$$\alpha = 9f \frac{\omega \varepsilon_B^{3/2}}{c} \frac{\varepsilon_2}{(\varepsilon_1 + 2\varepsilon_B)^2 + \varepsilon_2^2}$$

where ε_1 and ε_2 are real and imaginary parts of ε_A [17]. This absorption coefficient has a maximum at ω for which the condition $\varepsilon_1 + 2\varepsilon_B = 0$ takes place, which is known as the surface plasmon resonance.

In the aggregate topology the ESU are two spheres (Figure 7.1b). These two spheres are submerged into the effective medium, and their relative concentrations are f and $1 - f$, where f is a volume fraction of the constituent A. Using the dipolar approximation of $S(\theta)$ for a sphere [12] leads to the Bruggeman equation:

$$f\frac{\varepsilon_B-\varepsilon_{\text{eff}}}{\varepsilon_B+2\varepsilon_{\text{eff}}}+(1-f)\frac{\varepsilon_A-\varepsilon_{\text{eff}}}{\varepsilon_A+2\varepsilon_{\text{eff}}}=0 \tag{3}$$

For small concentrations of inclusions (f close to 1 or to 0), it appears that a number of composite films are better described by the separated grain structure—that is, ruled by the MG equation. For intermediate values of f, the BG approach gives better results. Nevertheless, both approaches are not very precise. That is why symmetrized MG approximations have been proposed by introducing an average over the two following random units: an inclusion of A coated by a shell of B and an inclusion of B coated by a shell of A. Using this picture, the film or plate can be modeled as a mixture of two types of coated spheres or ellipsoids. Dielectric-coated metal ellipsoids are denoted as type 1 units, and metal-coated insulator ellipsoids are denoted as type 2 units (Figure 7.2). The problem is to evaluate the proportion of these two random units for a given value of the filling factor f. Sheng [4] has introduced a probabilistic growth model where the probability of occurrence of these two units as a function of f is given by the number of possible configurations of each type of units. This number is given by the volume available to the internal ellipsoid in the external ellipsoid. For details see reference 4.

2.2. The Hanai–Bruggeman Formula

The HBG formulas, also known as the asymmetric Bruggeman formulas, are obtained assuming that the MG model is exact at low filling factors and then, following an iterative procedure, adding a small fraction of particles at each step [18, 19]. This model is recognized as valid at least for $f < 0.8$.

The first HBG formula is for spherical particles:

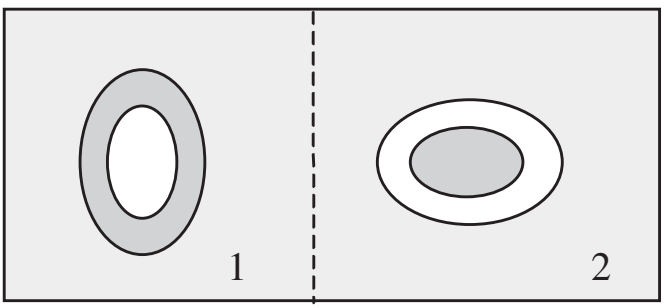

Figure 7.2. Random units 1 and 2 in the effective medium (symmetrized Maxwell Garnett approximation).

$$\frac{\varepsilon_2 - \varepsilon_{\text{eff}}}{\varepsilon_2 - \varepsilon_1}\left(\frac{\varepsilon_1}{\varepsilon_{\text{eff}}}\right)^{1/3} = 1 - f$$

and the second one is for lamellar particles:

$$\varepsilon_{\text{eff}} = \varepsilon_2 \frac{3\varepsilon_1 + 2f(\varepsilon_2 - \varepsilon_1)}{\varepsilon_2 - f(\varepsilon_2 - \varepsilon_1)}$$

Some authors have proposed a generalized HBG equation that includes all possible types of inclusion geometry [20]:

$$\frac{\varepsilon_2 - \varepsilon_{\text{eff}}}{\varepsilon_2 - \varepsilon_1}\left(\frac{\varepsilon_1}{\varepsilon_{\text{eff}}}\right)^{L} = 1 - f$$

The generalization is accomplished by letting the depolarization factor L vary between 0 and 1.

Thus, if the wavelength of the light is much greater than the grain size, the long wavelength approximation and effective medium theory can be applied to determine the effective value of the composite dielectric constant and, consequently, describe composites optical properties. However, if the size of the structure is of the order of tens and even units of nanometers, then the effective medium approach is not applicable. Indeed, within this approximation, the effective permittivity of a composite is determined as a function of the permittivity for each composite component and, in turn, the nanocomposite components are characterized by the same tensor of permittivity as those used for bulk media.[1]

[1] However, in the case of granular metallic structures in which the grain sizes do not exceed several nanometers, the conditions of applicability of this approach are violated, because the mean free path of electrons in these materials is considerably greater than the mean grain size, and spin-dependent scattering and tunneling of electrons become significant. Thus, it is evident that the effective-medium approximation, as applied to these systems, is rather contradictory and does not offer an adequate description of their properties. For the optical properties of the composites with magnetic constituents, spin-dependent electron scattering both inside conducting regions and at rough interfaces plays a very important role. The only way to describe optical properties of the composite in such a case is to consider directly an interaction of light and electrons in the composite. It can be done, for example, by means of the consistent solution of Boltzmann kinetic equation in each region of the material. This procedure is rather complex and can be done exactly only for some special composite geometries: spherical inclusions in the uniform matrix or multilayered film [21, 22]. Since the electron distribution function is found, the current distribution can be readily calculated and after using the averaging procedure one can determine dielectric constant for the material. Some other theoretical approaches can be found in references 23–25.

If we are interested not only in the total optical response of the medium but also in its response at submicron scales and nanoscales (i.e., imaging of the nanosized structures), then it is vital to have a possibility of calculation of fine electromagnetic field distribution at the fixed distances above the sample. One of the powerful methods that can be utilized for that is the Green function technique, which will be described in Section 7.

2.3. Effective Medium Approach for Magnetic Composites

Basic equations of the homogenization theory are applicable not only for scalar values of the constituents dielectric constants ε_i, but also for the tensorial quantities. Indeed, evaluation of these equations does not demand any special requirements regarding the character of the electric displacement D and electric intensity E relation: $D = \hat{\varepsilon}\varepsilon_0 E$ in which dielectric constant $\hat{\varepsilon}$ can be tensorial. This fact enables us to calculate the effective dielectric constant ε_{eff} for the composites with anisotropic constituents. It can be, for example, polymer composites with magnetic granular, the permittivity of which is tensorial quantity. The explicit form of the $\hat{\varepsilon}$ tensor for magnetic media will be given in the next section.

Here we consider effective-medium equations for a composite consisting of the anisotropic granules characterized by permittivity $\hat{\varepsilon}_A$ placed into an isotropic matrix with permittivity $\varepsilon_B\hat{I}$, where $\hat{I}$ is the unit tensor.

We assume that the anisotropic part of $\hat{\varepsilon}_A$ tensor, which we denote as $\delta\hat{\varepsilon}_A$, is much smaller than the diagonal one. Thus, $\hat{\varepsilon}_A$ tensor can be presented as

$$\hat{\varepsilon}_A = \varepsilon_A\hat{\mathrm{I}} + \delta\hat{\varepsilon}_A$$

where $|\delta\hat{\varepsilon}_A| \ll \varepsilon_A$. Effective permittivity $\hat{\varepsilon}_{\text{eff}}$ can also be written in the form $\hat{\varepsilon}_{\text{eff}} = \varepsilon_{\text{eff}}\hat{\mathrm{I}} + \delta\hat{\varepsilon}_{\text{eff}}$. The anisotropic part of the $\hat{\varepsilon}_{\text{eff}}$ tensor is to be found from the conventional mixture equations. Substitution of the tensorial form of the phase permittivities into the MG equation (2) gives

$$\delta\hat{\varepsilon}_{\text{eff}} = \left(\frac{3\varepsilon_B\sqrt{f}}{\varepsilon_A(1-f)+\varepsilon_B(2+f)}\right)^2 \delta\hat{\varepsilon}_A \tag{4}$$

If the $\delta\hat{\varepsilon}_A$ tensor has only off-diagonal nonzero components, then the Bruggeman equation leads to the following expression for $\delta\hat{\varepsilon}_{\text{eff}}$:

$$\delta\hat{\varepsilon}_{\text{eff}} = \frac{f\varepsilon_{\text{eff}}\delta\varepsilon_A}{(\varepsilon_A+2\varepsilon_{\text{eff}})^2} \Bigg/ \left[f\frac{\varepsilon_A}{(\varepsilon_A+2\varepsilon_{\text{eff}})^2} + (1-f)\frac{\varepsilon_B}{(\varepsilon_B+2\varepsilon_{\text{eff}})^2}\right] \tag{5}$$

ε_{eff} is to be found from the conventional BG equation (3). The BG approach also works for the case when some diagonal components of the $\delta\hat{\varepsilon}_A$ tensor are nonzero, but this time expression for $\delta\hat{\varepsilon}_{\text{eff}}$ is more cumbersome.

Since equation (4) was derived from the MG equation, it is applicable for small concentrations of inclusions. On the contrary, equation (5), which was derived from the BG equation, is more appropriate for the intermediate values of f.

Determination of the $\delta\hat{\varepsilon}_{\text{eff}}$ tensor allows us to describe anisotropic optical properties of the composites. In particular, for magnetic composites the effective value of the MO parameter Q, which plays an important role in the magnetooptics, can be evaluated. The definition of the parameter Q is given in the next section.

3. MAGNETOOPTICS OF UNIFORM MEDIA

Particular properties of a medium in the macroscopic theory of the MO phenomena are defined by the form of the $\hat{\varepsilon}$ and $\hat{\mu}$ tensors. It is enough to consider just the $\hat{\varepsilon}$ tensor, because the properties that we describe below are similar for $\hat{\varepsilon}$ and $\hat{\mu}$ tensors. Besides, for visible and near-infrared light the $\hat{\mu}$ tensor is approximately equal to the unit tensor. In the magnetically ordered state the $\hat{\varepsilon}$ tensor depends on the order parameter. In ferromagnets the order parameter is magnetization M, in antiferromagnets it is the sublattice magnetization, and so on. We shall confine our discussion to ferromagnets.

Let us consider the simplest case of an optically isotropic ferromagnet. The presence of magnetization reduces the symmetry to the single-axis one. The $\hat{\varepsilon}$ tensor can be represented as a sum of symmetric and asymmetric tensors, which is given by [26]

$$\hat{\varepsilon} = \begin{pmatrix} \varepsilon_1 & 0 & 0 \\ 0 & \varepsilon_1 & 0 \\ 0 & 0 & \varepsilon_0 \end{pmatrix} + ig \begin{pmatrix} 0 & -m_z & m_y \\ m_z & 0 & -m_x \\ -m_y & m_x & 0 \end{pmatrix} \tag{6}$$

The D vector for ferromagnetic medium can be written as

$$D = \varepsilon_0 E + i[g \times E] + b(E - m(m \cdot E)), \tag{7}$$

where $m = M/M$, $b(M) = \varepsilon_1 - \varepsilon_0$, ε_0 is the dielectric permittivity of the medium at $M = 0$, and g is the gyration vector. In an isotropic medium, normally $g = aM$. If there is an absorption, then

$$\varepsilon_0 = \varepsilon_0' + i\varepsilon_0'', \qquad g = g' + ig'', \qquad b = b' + ib''$$

are complex functions of the frequency. The second terms in the formulas (6) and (7) define the gyrotropic effects: magnetic gyrotropic birefringence and magnetic circular dichroism. The last terms define optical magnetic anisotropy: magnetic linear birefringence and magnetic linear dichroism.

The constants g and b become zero when M approaches zero.

Usually for the characterization of the MO effects the MO (Voigt) parameter Q is used. It is defined as

$$Q = Q' + iQ'' = g/\varepsilon_1$$

Normally, $|Q| \ll 1$. If the $\hat{\mu}$ tensor can no longer be considered as a unit tensor, then both Q and Q_M need to taken into account and the MO medium is called bi-gyrotropic.

In crystals the dependence of the $\hat{\varepsilon}$ tensor on M is more complicated, namely,

$$\varepsilon_{ik} = \varepsilon_{ik}^0 - ie_{ikl}g_l + \delta_{iklm}M_lM_m$$

where $g_l = a_{lq}M_q$ and e_{ikl} is the antisymmetric three-dimensional-order pseudotensor (the Levi–Civita tensor). The polar tensors ε_{ik}^0, a_{lq}, and δ_{iklm} are defined by the crystallographic symmetry.

4. MAGNETOOPTICAL EFFECTS IN TRANSMISSION

The MO Faraday effect manifests itself in a rotation of polarization plane of a linearly polarized light at an angle Φ when the light propagates along the medium magnetization M (Figure 7.3).

In electromagnetic theory the Faraday effect can be explained as follows. When the medium magnetization has non-zero projection on the wave vector k_0 of the incident radiation, two independent fundamental Maxwell equations solutions are circular polarized waves with different refractive indexes n_+ и n_-, respectively. At the output of the magnetic medium these waves gain phase shift and when added give linearly polarized wave with rotated polarization plane. That is why Faraday effect is also called magnetic circular birefringence [26, 27].

The angle of the light polarization plane rotation is given by

$$\theta = \theta_F h = -\frac{k_0 g h}{2n_0}$$

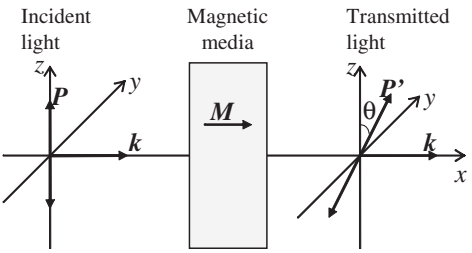

Figure 7.3. The MO effect resulting from the interaction of optical radiation with the medium for the geometry when radiation passes along the medium magnetization—the Faraday effect.

where θ_F is a specific Faraday rotation (rotation of polarization plane of the wave per unit length of the sample, typical values of θ_F are 1000–30,000°/sm), $n_0 = {}^1\!/_2(n_+ + n_-)$, h is the sample's thickness, k_0 is the wave vector module of the incident light, and g is the module of the medium gyration vector [26].

If a medium has absorption, the absorption coefficients of the right- and left-handed circular polarized light are different. This phenomenon is called *magnetic circular dichroism*. After transmission through a medium that exhibits such properties, the light changes its polarization from linear to elliptical. The elliptical polarization is characterized by the orientation angle θ, which is analogous to the Faraday angle, and ellipticity ψ. These quantities are calculated by [26]

$$\theta = -\frac{k_0 g' h}{2n_0}, \qquad \psi = -\frac{k_0 g'' h}{2n_0}$$

Specific magnetic circular birefringence and magnetic circular dichroism can be unified into one general concept—the complex specific Faraday rotation:

$$\tilde{\theta}_F = \theta_F + i\psi_F = -\frac{k_0 g h}{2n_0}$$

The Faraday effect is widely used for the magnetic structure visualization in transparent samples with an easy direction axis not parallel to the sample's surface [27]. In this case, electromagnetic radiation passing through the domains of opposite magnetization gains slightly different rotation of the polarization plane. This enables us to visualize domains and domain walls by means

of analyzer. Depending on the mutual orientation of polarizer and analyzer, one can obtain images with different types of the contrast (Figure 7.4).

If the magnetic sample is transparent but magnetized in its plane, then for the visualization of the magnetic structure the Cotton–Mouton or Voigt effect can be used. It arises when electromagnetic radiation propagates in the direction that is perpendicular to the medium's magnetization. A linearly polarized light that has its polarization plane oriented at an angle to the magnetization direction becomes elliptically polarized after propagation through the medium, with the longer axes of the ellipse being approximately parallel to the incident polarization. This effect results from the difference of refractive indexes of two components of light radiation, which are linearly polarized parallel and perpendicular to the direction of magnetization. Consequently, magnetic linear birefringence takes place.

The Voigt effect is often revealed in experiment as a relative phase shift of the two polarization components per unit length of a sample:

$$B_{C-M} = (\omega/c)|\mathrm{Re}(n_{\|} - n_{\perp})|$$

where $n_{\|} = (\varepsilon_0)^{1/2}$ and $n_{\perp} = (\varepsilon_1 - \varepsilon_0^{-1} g^2)^{1/2}$ are the refractive indexes for the light polarized parallel and perpendicular to the gyration vector.

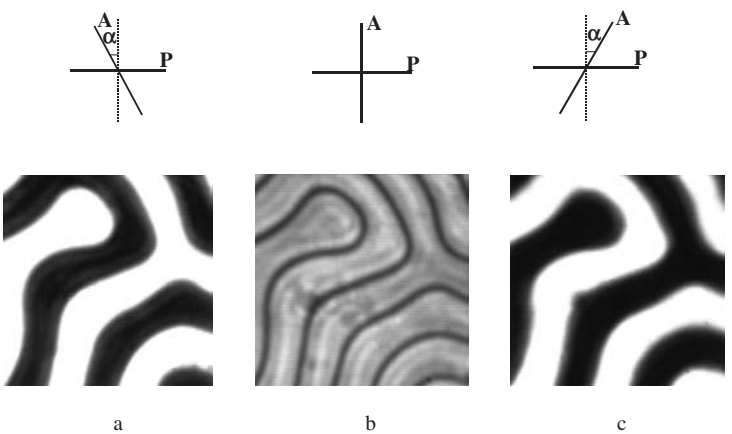

Figure 7.4. Domains images in the polarization microscopy (the field of vision size is 20 mkm) at the different mutual positions of polarizer and analyzer: **(a, c)** Domain contrast; **(b)** domain walls contrast. In the inlets mutual polarizer (P), analyzer (A) orientations are showed.

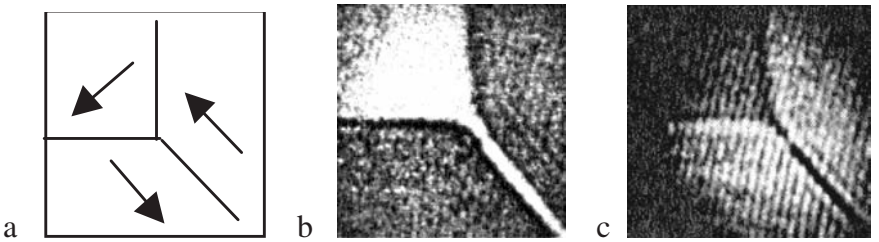

Figure 7.5. Domain structure observation by means of the Cotton–Mouton effect in the iron–garnet film with crystallographic orientation (100). (**a**) Magnetization distribution in the sample; (**b, c**) images obtained at different polarizer and analyzer orientations [28].

The Voigt effect is quadratic in magnetization (i.e., the second-order effect), in contrast to the Faraday effect, which is linear in magnetization.

Analogous to circular magnetic dichroism, linear magnetic dichroism is also possible in absorbing medium. This effect originates from the difference in absorption coefficients of the two fundamental linearly polarized waves. The presence of the magnetic linear dichroism results in a rotation of the orientational angle of the ellipse during the wave propagation.

When the Voigt effect is utilized for the sample's magnetic pattern observation, the analyzer half-wave plate is set in order to convert elliptical polarization into either linear polarization or new elliptical polarization, with the smaller eccentricity depending on the sign of rotation in the incident ellipse [28]. The polarization transformation courses differ in terms of the images of differently magnetized domains (Figure 7.5).

5. THE MAGNETOOPTICAL KERR EFFECT

Along with MO effects that take place during transmission of light through a magnetized substance, there are a number of effects that manifest themselves when the light is reflected from the surface of a magnetized material. These phenomena are conventionally designated MO Kerr effects (MOKE). There are three types of the Kerr effect, which are differentiated depending on a mutual orientation of the magnetization, with respect to both the wave propagation direction and the normal to the surface [26, 29].

The complex polar Kerr effect consists of both the rotation of polarization plane and the appearance of the ellipticity if a linearly polarized light reflects from a sample surface and the sample is magnetized normally to this surface (Figure 7.6a). If the light falls from the vacuum perpendicularly on the sample

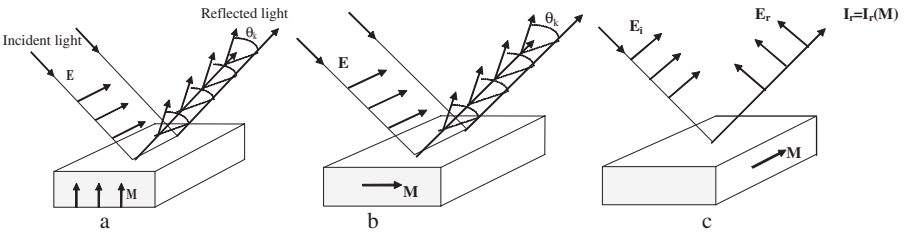

Figure 7.6. MO Kerr effects taking place when light is reflected from the surface of a magnetized material: polar (**a**), longitudinal (**b**), and transverse (**c**) effects.

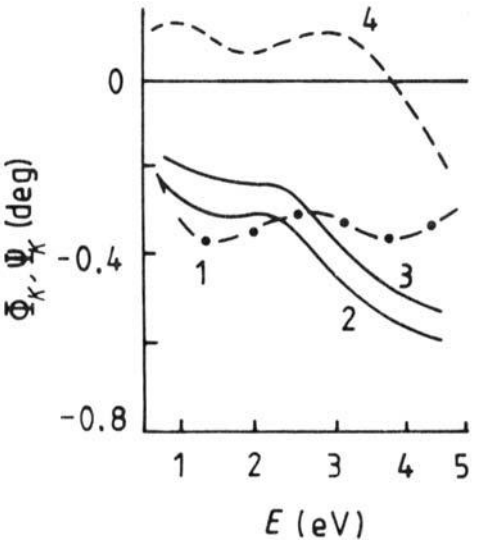

Figure 7.7. The polar Kerr rotation (curve 1) and the ellipticity (curve 2) for EuO single crystal at 10 K and $H = 40$ kOe [31].

surface, the expression for the complex polar Kerr effect takes the following form:

$$\tilde{\Phi}_K = \Phi_K + i\Psi_K = \frac{inQ}{n^2 - 1}$$

where Φ_K is the Kerr rotation angle and Ψ_K is the ellipticity. The polar Kerr effect versus photon energy is presented in Figure 7.7.

The longitudinal (meridional) Kerr effect means both the rotation of polarization plane and appearance of the ellipticity when a linearly polarized light

reflects from a sample surface provided that the magnetization vector belongs to both the sample plane and the light incidence plane (Figure 7.6b).

The polar and longitudinal Kerr effects constitute the group of longitudinal MO effects. Under certain conditions, variations of the intensity of linearly polarized reflected light are observed in the configuration of either the polar or longitudinal Kerr effect geometry [30].

Like the above-mentioned effects, the transversal (equatorial) Kerr effect is linear on magnetization. The transversal effect may be observed only in absorbing materials. It is manifested as the intensity variations and the phase shift of a linearly polarized light reflected from a magnetized material, if the magnetization lies in the sample plane but is perpendicular to the light incidence plane (Figure 7.6c). For p-polarization of the incident light (radiation polarization is perpendicular to the incident plane) the relative change in the reflected light intensity is given by

$$\delta_p = \frac{I - I_0}{I_0} = 2\,\mathrm{Im}\rho_{12}^{\mathrm{p}}$$

where I and I_0 are the intensities of the reflected light in the magnetized and nonmagnetized states, respectively,

$$\rho_{12}^{p} = \frac{r_{12}^{p} Q \sin\varphi}{2\left(n^2 - \sin^2\varphi\right)^{1/2}}$$

r_{12}^{p} is the conventional Fresnel coefficient for reflection, and n is the refraction coefficient for the magnetic medium.

MO Kerr effects are used to observe the domain structure of opaque materials. If the magnetization vector is perpendicular to the sample plane, then the polar Kerr effect is utilized. If the magnetization lies in the sample plane, then structure images can be obtained either in the longitudinal geometry with polarizers or in the transverse geometry without polarizers.

6. NONLINEAR MAGNETOOPTICAL EFFECTS

Nonlinear MO effects and, in particular, the second harmonic generation effect are becoming increasingly important because they are nondestructive and can be remotely sensed *in situ* with high spatial and temporal resolution at any interface accessible by light.

In centrosymmetric media, the electric field contribution to the second-order optical polararizability is forbidden by symmetry [32]. At the same time,

the majority of widely spread magnetic materials (Fe, Co, Ni, FeNi, etc.) possess inversion symmetry, so second harmonic generation appears only in ultrathin surface layer where inversion symmetry is broken. The magnetization of a material does not usually break this symmetry, but it can modify substantially the form of the nonlinear susceptibility for surface second harmonics generation [33, 34]. This explains the fact that nonlinear MO effects usually exceed corresponding linear effects by several orders of magnitude [35–42]. Thus for granular Co–Cu magnetic films (thickness is 200 nm) in polar geometry the nonlinear Kerr effect is 8°, whereas the linear effect is no more than several tenths of a degree [38]. In the transversal configuration the nonlinear effect surpasses the linear effect more than 40-fold. While investigating ultrathin films (thickness of 1–10 nm) it was revealed that the nonlinear effect, in contrast to the linear one, practically does not depend on the sample thickness and even for nanometer scales is about 10°–20° [39] (Figure 7.8). Thus, the technique of nonlinear optical signal observation is very convenient and sensitive for investigation of the magnetic materials surfaces.

The surface nonlinear optical polarization of second order can be written in the form [34]

$$P_s^{2\omega} = \chi_{ijk}^{(2)} E_j E_k \tag{8}$$

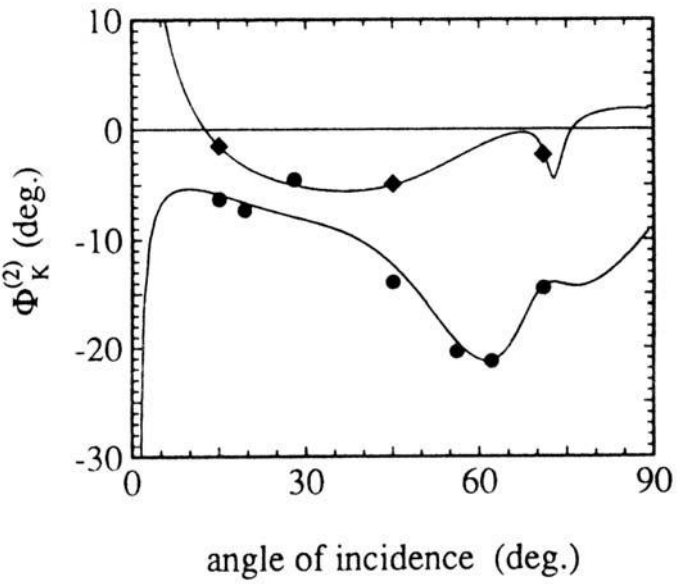

Figure 7.8. Nonlinear Kerr rotation $\Phi_k^{(2)}$ for an Fe–Cr multilayer as a function of the angle of incidence. Filled circles: s-input polarization; filled diamonds: p-input polarization. The curves are theoretical fits [39].

where the surface nonlinear susceptibility tensor $\chi_{ijk}^{(2)}$ is a function of magnetization M, and E is the electric field of the light wave. The symmetry of $\chi_{ijk}^{(2)}$ is defined by the time-reversal symmetry and by the symmetry of the particular surface under consideration. The time-reversal properties, neglecting dissipation, requires that the real part of $\chi_{ijk}^{(2)}$ is an even function of M, while the imaginary part is an odd function of M. The latter feature can be particularly useful for probing of the magnets surfaces.

From a symmetry viewpoint the second-order surface polarization in the linear (-in-M) approach can be written as

$$P_s^{2\omega} = P_{s0}^{2\omega} + P_{sm}^{2\omega} \tag{9}$$

where

$$P_{s0}^{2\omega} = \chi_1 E(EN) + \chi_2 E^2 N \tag{10}$$

and

$$P_{sm}^{2\omega} = \chi_3 E(E(mN)) + \chi_4 E^2 [mN] + \chi_5 [Em](EN) + \chi_6 [EN](Em) \tag{11}$$

are contributions that are independent of the magnetization $P_{s0}^{2\omega}$ and are linear in the magnetization $P_{sm}^{2\omega}$, where χ_i, $i = 1, 2$, are nonlinear optical parameters, and χ_i, $i = 3, 4, 5, 6$, are nonlinear MO parameters; and N is the vector normal to the surface. It is clear that only these two independent combinations that are second order in E and have the symmetry of the polar vector can be composed from the polar vectors N and E to get $P_{s0}^{2\omega}$; and only four independent combinations can be composed from the polar vectors N and E and the axial vector m to get $P_{sm}^{2\omega}$.

The relation (11) should be regarded as an expansion of $P(E, N, M)$ in E, N, and M. We restrict the analysis to the terms that are quadratic in E and linear in N and M. The ratio of the light-wave field E to the magnitude of the intraatomic field E^*, the ratio $\zeta = E_{surf}/E^*$ of the surface electric field E_{surf} (which breaks the even symmetry at the surface) to E^* (for N), and the magnitude of the magnetooptical gyrotropy (M), which is determined by the MO parameter Q and usually satisfies the condition $Q \ll 1$, are small parameters. Here expansion in N actually means expansion in NE_{surf}, as was shown in reference 35.

The use of the expansions (10) and (11) reduces the number of parameters needed to describe nonlinear MO phenomena (in comparison to the general formula (8). We can show this by comparing equation (8) with equations (9) and (10). Formula (10) can naturally be represented in a matrix form, just as equation (8), where the third-rank tensor has the following form in Voigt's notation:

$$\begin{bmatrix} 0 & 0 & 0 & 0 & e_{15} & 0 \\ 0 & 0 & 0 & e_{15} & 0 & 0 \\ e_{31} & e_{31} & e_{33} & 0 & 0 & 0 \end{bmatrix} \tag{12}$$

It is symmetric relative to interchange of the indices j and k. Such a form for the tensor $\chi^{(2)}_{ijk}$ corresponds to the limiting ∞m symmetry group (the Curie group). A uniform electric field, for example, has this symmetry. It follows from equation (10) that $e_{33} = e_{31} + 2e_{15}$; that is, the tensor $\chi^{(2)}_{ijk}$ ($M = 0$) is specified in our case by two independent parameters, rather than three, as required by ∞m symmetry. However, there is no contradiction between formulas (10) and (11), since formula (10) corresponds to the linear approximation with respect to z. Taking into account the next term with respect to z in the expansion in (10) in, for example, the form $N(NE)^2$, we obtain $e_{33} = e_{31} + 2e_{15} + O(\zeta^2)$.

7. GREEN FUNCTIONS APPROACH. OPTICS OF SEPARATE NANOOBJECTS

Averaged signal from inhomogeneous medium with nanoscaled objects generally is not very informative, and it is vital in some cases to detect signal from separate nanostructures. This type of situation arises, for example, in read–write processes at high storage densities, when the sizes of the written information bits and distances between them do not exceed several tens of nanometers. At this stage, characterization of the optical properties of the sample by the effective permittivity is no longer appropriate, and one has to use methods more rigorous than the homogenization technique. Among these methods, the dyadic Green functions approach deserves particular consideration.

As is known from the differential equations theory, the Green functions are used for solution of the linear inhomogeneous differential equations:

$$\hat{L}_{\psi(r)} = f(r) \tag{13}$$

where $\hat{L}$ is the linear differential operator. The Green function for this equation is given by

$$\hat{L}G(r, r') = \delta(r - r')$$

With the use of the Green function, the solution of equation (13) can be expressed as

$$\psi(r) = \psi_0(r) + \int G(r, r') f(r') dr',$$

where $\psi_0(r)$ is the solution of corresponding homogeneous equation. The standard Helmholtz equation with nonzero right side

$$\Delta E(r) + k_0^2 E(r) = F(r)$$

where $k_0 = \omega/c$, can be solved in terms of the function

$$G(r, r') = \frac{e^{ik_0|r-r'|}}{|r-r'|}$$

which is called the *scalar free-space Green function*.

However, while dealing with the inhomogeneous medium, one faces more complex equation. The medium inhomogeneities can be described by a relatively small additional term $P_1(r,t)$ in the medium polarization:

$$P(r,t) = \varepsilon_0 \chi(z,\omega) E(r,t) + P_1(r,t)$$

The fact that susceptibility $\chi(z,\omega)$ depends only on the Z-spatial coordinate means that we examine here a medium with a stratified structure. The polarization vector $P_1(r,t)$ is determined by the kind of inhomogeneities. If it is related to the magnetization distribution, then in linear magnetooptics we have

$$P_1(r,t) = i\varepsilon_0 \varepsilon Q \cdot m \times E(r,t)$$

where $m = M/M$ is the unit magnetization vector and Q is the MO parameter (see Section 3). If one is to investigate the MO response at the second harmonics, then $P_1(r,t)$ is determined by equation (8).

In the Maxwell equation

$$\nabla \times \nabla \times E(r,t) = -\mu_0 \frac{\partial^2}{\partial t^2} D(r,t)$$

let us substitute $E(r,t) = E(r,\omega)e^{-i\omega t}$ and $D(r,t) = D(r,\omega)e^{-i\omega t}$ and use the relation

$$D(r,\omega) = \varepsilon_0 E(r,\omega) + P(r,\omega) = \varepsilon_0 \varepsilon(z,\omega) E(r,\omega) + P_1(r,\omega)$$

where $\varepsilon(z,\omega) = 1 + \chi(z,\omega)$. Then the equation for the Fourier coefficient of the electric field $E(r,\omega)$ is given by

$$\nabla \times \nabla \times E(r,\omega) - \varepsilon(z,\omega) k_0^2 E(r,\omega) = \frac{k_0^2}{\varepsilon_0} P_1(r,\omega) \tag{14}$$

where $k_0 = \omega/c$. This equation is inhomogeneous, and thus the apparatus of the Green function can be used to solve it. But the Green function this time is dyadic [43]. It is introduced by the equations

$$\left(\frac{\partial^2}{\partial x_\lambda \partial x_\mu} - \delta_{\lambda\mu}\frac{\partial^2}{\partial x_\mu^2} - \varepsilon(r)\frac{\omega_0^2}{c^2}\delta_{\lambda\mu}\right)G_{\mu\nu}(r, r', \omega) = -\delta_{\lambda\nu}\delta(r - r') \qquad (15)$$

which are solved with ordinary Maxwell boundary conditions. Therefore, the expressions for the fields derived using the Green function *a priori* meet these boundary conditions. The method of Green functions makes it possible to derive analytical formulas for the Fourier transform of the electric field of a diffracted wave. This approach proved to be valid in solving a great variety of scattering problems: light reflection and transmission in rough surface media [43, 44], plasmon polariton propagation [45], investigation of nonlinear surface MO effects [36, 40], and calculation of the field distribution in the near-field region [46–49].

With the use of this function, one can convert the partial differential equation (14) into an integral equation

$$E_\mu(r, \omega) = E_\mu^{(0)}(r, \omega) - \frac{k_0^2}{\varepsilon_0}\int d^3r' G_{\mu\nu}(r, r', \omega)P_{1\nu}(r, \omega), \qquad (16)$$

where $E_\mu^{(0)}(r,\omega)$ is a solution of the corresponding homogeneous equation

$$\nabla \times \nabla \times E(r, \omega) - \varepsilon(z, \omega)k_0^2 E(r, \omega) = 0$$

$E_\mu^{(0)}(r,\omega)$ describes electric field without taking into account inhomogeneities. To solve the integral equation (16), the first Born approximation can be utilized. In the first Born approximation, additional medium polarization $P_1(r,\omega)$ depends only on the unperturbed electric field $E_\mu^{(0)}(r,\omega)$, and the total electric field is

$$E_\mu(r, \omega) = E_\mu^{(0)}(r, \omega) + E_\mu^{(1)}(r, \omega)$$

where $E_\mu^{(1)}(r, \omega) = -\frac{k_0^2}{\varepsilon_0}\int d^3r' G_{\mu\nu}(r, r', \omega)P_{1\nu}^{(0)}(r', \omega)$

To proceed further, it is appropriate to introduce the Fourier representations of $G_{\mu\nu}(r,r',\omega)$ and $P_{1\nu}^{(0)}(r,\omega)$:

$$G_{\mu\nu}(r, r', \omega) = \frac{1}{4\pi^2}\int d^2k_{||} \exp(ik_{||}(r_{||} - r_{||}'))g_{\mu\nu}(z, z', \omega, k_{||}) \qquad (17)$$

$$P_{1\nu}^{(0)}(r,\omega)=\frac{1}{4\pi^2}\int d^2k_{\|}\exp(ik_{\|}r_{\|})\hat{P}_{1\nu}^{(0)}(z,\omega,k_{\|}) \tag{18}$$

where $k_{\|}=(k_x,k_y,0)$ and $r_{\|}=(x,y,0)$. The form of these representations is dictated by the dielectric constant $\varepsilon(z,\omega)$. The Fourier transforms of the Green functions are determined by solving ordinary differential equations. This procedure is outlined, for example, in references 43–45. Examples of the Green function Fourier transforms for the half-space or plate can be found in references 43 and 45.

Using equations (17) and (18), we can express Fourier transform of the scattered electric field $\hat{E}_{\mu}^{(1)}(z,\omega,k_{\|})$ in terms of the Fourier transform $\hat{P}_{1\nu}^{(0)}(z,\omega,k_{\|})$ of the medium inhomogeneities polarization:

$$\hat{E}_{\mu}^{(1)}(z,\omega,k_{\|})=-\frac{k_0^2}{16\pi^4}\int dz' g_{\mu\nu}(z,z',\omega,k_{\|})\hat{P}_{1\nu}(z',\omega,k_{\|}) \tag{19}$$

Thus, to pass to the electric field distribution in the real space, one needs to make inverse Fourier transformation.

With the electric field $E(r,\omega)$ found, one can calculate optical properties of the material—transmission, reflection, and absorption—and simulate an image of its structure. For the letter, it is important that relation (19) describes in fact the angular spatial spectrum of the field of the wave diffracted from the grains or other inhomogeneities of the sample (e.g., magnetic structure). The scattered wave field can be written as a superposition of electromagnetic plane waves with various wave vectors $k_{\|}$ and complex amplitudes defined by equation (19). Based on equation (19), one can theoretically investigate optical properties of the materials and calculate images of their dielectric and magnetic structures obtained in the various types of the microscopy. Two examples of such calculations for the scanning near-field and dark-field microscopies are presented in Section 10. The microscopic image is formed by those spatial Fourier components of the wave field that arrive at the microscope objective. A set of harmonics passed through the system is controlled by the objective numerical aperture $NA = n\sin u$, where n is the refractive index of the medium surrounding the objective and u is the aperture angle of the objective. Thus, the features of the image formed in the optical system are controlled by the inverse Fourier transform that takes into account only the field harmonics passed through the system:

$$E_{\mu}^{(1)}=\frac{1}{4\pi^2}\int\limits_{\{k_{\|}\}} dk_{\|}\hat{E}_{\mu}^{(1)}e^{ik_{\|}r} \tag{20}$$

Once electric field at the image plane is found, one can calculate the intensity distribution at this plane: $I(r_{\|})=|E(r_{\|})|^2$; that is, one can simulate an image of the investigated structure.

8. SCANNING NEAR-FIELD OPTICAL MICROSCOPY

Detailed study of the magnetization distributions on submicrometer spatial scales and the elaboration of the corresponding high-resolution techniques is presently one of the most important problems in applied and fundamental micromagnetism. In the past decade, significant progress has been made in the development of methods for studying micro- and nanostructures with the advent and onrush of magnetic force microscopy, which is a version of scanning probe microscopy [50]. Currently, magnetic force microscopy is characterized by the best spatial resolution in studying magnetic microstructures (tens of nanometers [51]). However, its application offers a number of problems: complicated interpretation and identification of images, the uncontrollable influence of the microprobe on the magnetization distribution in samples and vice versa, the problem of positioning the force microscope tip above a surface point under study, and the low scanning velocity, which makes real-time observation of fast processes impossible [52]. In this connection, some other alternative methods of magnetic imaging should be investigated. In this chapter we shall analyze scope and limitations of the promising approach to optical microscopy of magnetic structures, namely, scanning near-field optical microscopy (SNOM). It combines the rich capabilities of optical methods with the high resolution of scanning probe microscopy [53, 54]. In the SNOM, a probe scans the specimen, with the distance between them being smaller than the wavelength from its surface.

The SNOM can be utilized in a variety of different imaging modes including illumination mode, collection mode and dual mode (Figure 7.9) [55, 56]. In all modes, the resolution depends on the aperture size and the probe-specimen spacing rather than on the wavelength. In the illumination mode, the probe acts as the optical near-field generator, which illuminates the specimen. The signal (transmitted, reflected, or emitted light) is collected in the far-field using conventional optics. In the collection mode of the SNOM, the sample is illuminated using far-field optics and the signal is collected by the SNOM tip. Both the illumination mode and the collection mode of the SNOM have been utilized and have achieved high-resolution imaging [53–58]. The motivation in choosing one imaging mode over another is usually dictated by the particular experiment. The tip can also be used to both illuminate the sample and to collect the signal, a configuration known as dual SNOM mode [59]. This arrangement is attractive because it is easy to implement (the need for far-field optics—that is, the conventional optical microscope—is eliminated). In this mode, however, both the illumination light and the collected signal must pass through the aperture, causing significant reduction in the signal-to-noise ratio.

Like conventional optical microscopy, the SNOM can be performed in transmission or in reflection. The most common method is the transmission SNOM in which a thin, transparent sample is excited by the tip (i.e., illumina-

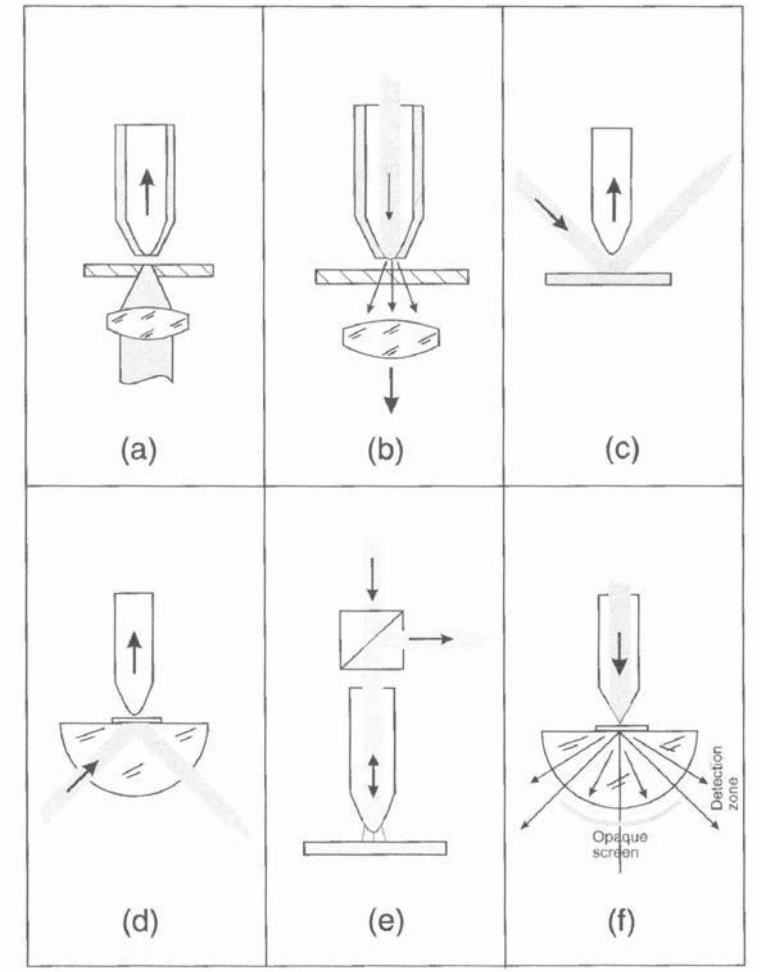

Figure 7.9. Types of the SNOM configurations. (**a**) Transmission collection mode. The tip is generally metallized except for its nano-sized end. (**b**) Transmission illumination mode. (**c**) Reflection collection mode. (**d**) Photon scanning tunnel mode. The illumination beam is totally reflected inside a substrate. (**e**) Dual illumination collection mode. It is a combination of (**a**) and (**b**). (**f**) Reflection illumination mode. It is an inverted photon tunnel mode (**d**) [53].

tion mode) and the signal light is collected in the far-field on the opposite side of the sample. For opaque samples, however, the reflection geometry is required. In the reflection SNOM, the tip and collection optics must be placed on the same side of the sample, which presents several important problems in comparison with transmission SNOM [60, 61].

Moreover, among SNOM modifications operating in the collection mode, there is a so-called photon scanning tunnel mode, where light is incident at the angle of total internal reflection (Figure 7.9d). The optical near field localized in the neighborhood of the specimen surface is detected with a near-field probe.

The first application of the SNOM for the MO studies happened in 1992 [62], when it was demonstrated that near-field MO observation can be obtained in the same manner as conventional far-field observation—that is, by using two cross-polarizers. Betzig et al. [62] visualized 100-nm magnetic domains and claimed spatial resolution of 30–50 nm. The possibility of MO domain imaging was confirmed in both the transmission regime (Faraday geometry) [63, 64] and the reflection regime (Kerr microscopy) [65–67].

By now the MO SNOM development is only at the initial stage. Published experimental results are not very numerous and mainly addressed the investigation of the simple magnetic structures in Co–Pt multilayers [62] and iron–garnet films [63–70]. Apart from that, some problems related to the MO images interpretation arise. At the same time, the MO SNOM has indisputable potential for the imaging of magnetic structures due to its high resolution unlimited by the light diffraction. That is why further experimental and theoretical work is essential. In particular, utilization of the computer simulation of the near-field images with some *a priori* model of the object with the subsequent comparison of simulated and observed images looks quite natural for overcoming the problem of images interpretation. In such simulation the dyadic Green function technique can be very fruitful. Let us consider its application for the calculation of magnetic nanoparticle images in SNOM.

We examine here the passive probe model [71], which ignores the effect of the probe on the SNOM image and assumes that the signal detected is proportional to the near-field intensity at the nanostructure surface in the absence of the probe. This hypothesis may be valid either if the field scattered by the tip is very small or if it is not reflected back by the sample. Thus, from this qualitative analysis, we may expect the probe to be passive either if the tip is very small or if the sample has a low reflectivity. Therefore, a metallic tip close to a metallic sample may not satisfy the assumption of a passive probe, whereas a tiny metallic tip above a dielectric (or magnetic) might be considered as a passive probe.

A passive probe model simplifies calculation substantially. Indeed, such an approach enables us to work in the first Born approximation, while for calculation of the near field we only need to calculate the scattered field $\hat{E}_{\mu}^{(1)}(z,\omega,k_{\|})$ by equation (19) with the Fourier transform $\hat{P}_{1v}^{(0)}(z,\omega,k_{\|})$ chosen to be compatible with the kind of nanoscaled structure. The specificity of work in the near-field reveals information on the domain of integration $\{k_{\|}\}$ in equation (20). Since the main idea of the SNOM lies in dealing with nonradiation evanescent waves that correspond to the high spatial frequencies, domain $\{k_{\|}\}$ must include

a wide range of $k_{\|}$, including $k_{\|}$ for which $|k_{\|}| > k_0$. The fulfillment of the last inequality is necessary to obtain a high spatial resolution. For example, a resolution of 10 nm, which is reachable by the SNOM, can be achieved if all spatial harmonics with $k_{x,y} \in (-25k_0, 25k_0)$ are integrated. We should note here that the scanning altitude [which is z in equation (19)] must not be larger than several tens of nanometers. A more detailed description of the Green function method application for the calculations in the near field can be found in reference 46. Some results of the images modeling are presented in Section 10.

9. POLARIZED ANISOTROPIC DARK-FIELD MICROSCOPY

Dark-field optical microscopy techniques feature significant potential for detecting and studying such magnetic formations as domain boundaries and substructures (Bloch lines, Bloch points) characterized by an intricate magnetization distribution and a characteristic size of tenths and hundredths of a micrometer. Dark-field optical microscopy is widely used in the studies of phase objects in physics, mineralogy, biology, and so on [72]. In the simplest version of this method, a sample is illuminated through a condenser with a diaphragmed center, so that the light flux incident onto the sample represents a hollow cone (Figure 7.10). If the objective aperture is smaller than the condenser aperture,

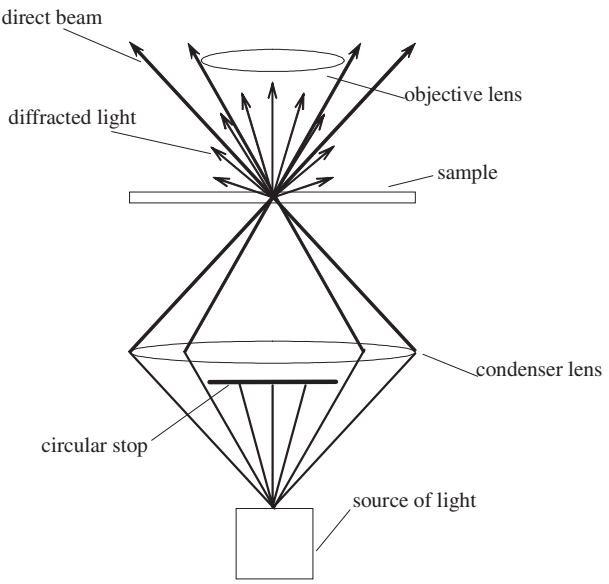

Figure 7.10. The schematic diagram of the phase-object observation using the dark-field method.

only light scattered at the sample phase structure hits the objective, forming a structure image.

In terms of the spatial resolution, the dark-field method is virtually equivalent to conventional optical microscopy [73]. At the same time, the detection sensitivity of the method under consideration is much higher than that of the conventional transmission microscopy, since the image is not subject to background illumination. This makes it possible to apply the dark field to observe and detect phase inhomogeneities smaller than or of the order of fractions of a micrometer (ultramicroscopy). Submicrometer magnetic structures may also be related to such phase inhomogeneities, because one can use the MO (Faraday, Kerr, Cotton–Mouton) effects. Currently, such magnetic structures also attract significant interest in the context of searches for new methods for data recording, storing, and reading.

The dark-field method was first applied to study magnetic media in reference 73, where the domain structure was visualized in ferrite–garnet films. A significant contribution to the development of MO dark-field microscopy was made by Thiaville and co-workers [74, 75], who optically detected the vertical Bloch lines (VBLs) in iron–garnet films and described the visualization mechanism.

The VBLs represent stable magnetic vortices and separate domain wall regions of opposite polarity [76]. The VBL sizes in many typical ferrite–garnet films do not exceed tenths of a micrometer.

In references 21 and 74–77, experiments were carried out using the anisotropic dark-field microscopy (ADFM) method, which is a modification of the conventional dark-field method wherein a narrow beam is cut out from the dark-field illumination cone. In references 74 and 75, the light incidence plane was normal to the domain wall planes (Figure 7.11).

In the ADFM images obtained in references 74 and 75 there is no illumination from domains, while domain walls are seen as contrast lines. Some portions of these lines exhibit lighter or darker regions, which are the VBLs of different magnetic topology (Figure 7.11). Further studies showed that the possibility of observing the Bloch lines in this dark-field configuration is related to the microscopic domain wall tilt in the VBL localization regions [21] rather than to light scattering immediately on the magnetization distribution in the Bloch line. Furthermore, another dark-field configuration making it possible to observe the Bloch lines is when the light incidence plane is parallel to the domain walls [21, 76, 77]. There is no illumination from either domains or domain walls in the images obtained in this configuration, while the VBLs are visualized as bright symmetric objects (Figure 7.11) regardless of magnetic topology.

The theoretical study reported in reference 78 allowed one to conclude that the VBL visualization mechanism in the last case is associated with light scattering on the VBL magnetic structure.

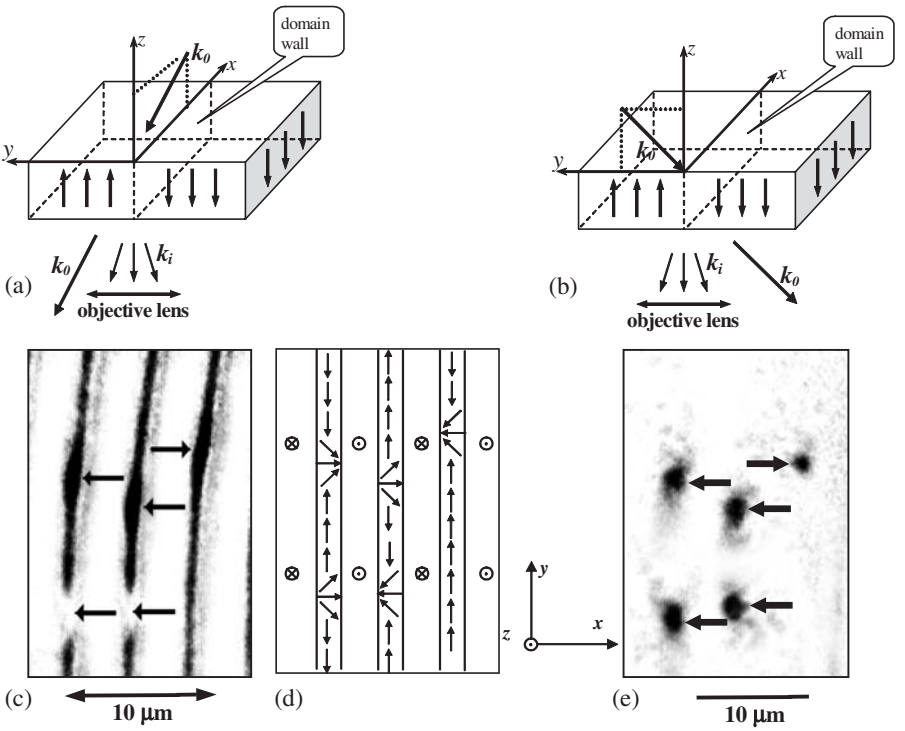

Figure 7.11. Observation of the VBLs in the ADFM. **(a, b)** Two main observation configurations. **(c, e)** Typical images of domain walls and Bloch lines (marked by arrows) obtained in observation configurations corresponding to **(a)** and **(b)**, respectively (contrast is inverted). **(d)** Magnetic structure of the sample. The Bloch lines are indicated by arrows.

Thus, the results obtained in references 74–79 showed that the dark-field method can be used to detect magnetic structures of size ~0.1 mkm. Varying the specific observation geometry (e.g., the angle of light incidence and the angle formed by the light incidence plane and the domain wall plane), it becomes possible to obtain various images of magnetic microstructures. In this case, the possibility of imaging through various mechanisms is not improbable.

The high sensitivity of the dark-field anisotropic observation method suggests its possible application for magnetic nanoparticles imaging that we discuss in brief in Section 10.

10. NANOSCALE MAGNETIC ELEMENTS, MAGNETIC DOTS IMAGING

In the bulk, ferromagnetic materials usually form domain structures to reduce their magnetostatic energy. However, in very small ferromagnetic systems—that is, magnetic dots with the diameter not exceeding several hundred nanometers, magnetic nanobridges, and nanowires—the formation of domain walls is not always energetically favored. Thus, in magnetic dots, some other configurations such as curling spin or collinear-spin configurations arise instead of the domain structure. If the dot thickness is much smaller than its diameter, then, as a rule, the following magnetization configuration takes place. Magnetization directions change gradually in-plane so as not to lose too much exchange energy, but to cancel the total dipole energy. In the vicinity of the dot center, the angle between adjacent spins then becomes increasingly larger when the spin directions remain confined in-plane. Therefore, at the core of the vortex structure, the magnetization turns out-of-plane and parallel to the plane normal [80, 81]. Calculations based on the discrete Monte Carlo method [82] or on the solving of the Landau–Lifshitz equation with the full-scale magneto-dipole interaction [83, 84] show that no out-of-plane component of the magnetization occurs if the dot thickness becomes too small. When the thickness exceeds a certain limit, the top and bottom spin layers will tend to cancel each other, and again no perpendicular magnetization should be observed. For the dots with diameters smaller than 100 nm, a collinear-type single-domain phase is energy-wise preferable. So with respect to the size and shape of the magnetic dots, different magnetic structures are realized.

Furthermore, many interesting and not always predictable spin configurations happen in the dynamics when the external magnetic field is applied [83].

Though there are some other methods for the investigation of magnetization structures at the nanometer scales (magnetic force microscopy, spin tunnel microscopy), the MO observation can also give much information.

One of the MO methods that can be suitable here is the MOKE (Section 5)-based measurement of the hysteresis loops by plotting the signal (rotation or ellipticity) as a function of the applied magnetic field [85–87]. Cowburn et al. [87] reported such measurements at the longitudinal MOKE on nanoscale supermalloy ($Ni_{80}Fe_{14}$–Mo_5) dot arrays. From their experiments it was possible to conclude that a collinear-type single-domain phase is established in the particles with diameters smaller than a critical value (about 100 nm) and that a vortex phase likely occurs in dots with larger diameters. Aign et al. [88] used polar MO Kerr microscopy to show the influence of dipolar interaction on the magnetization reversal in the individual Co dots and on the collective behavior of the dots array. From a comprehensive MO microscopy study, coupled to

numerical simulations, they arrived at a detailed understanding of the parameters that drive the single dot and collective magnetization reversal behaviors, as, for instance, the formation of magnetostatically frustrated zones in the arrays.

Investigation of magnetic nanoobjects structure on ultrafast timescales is possible with the use of stroboscopic effects [89–91]. Domain walls propagation in magnetic nanowires was also observed by the MOKE microscopy [92]. Thus among the variety of MO methods the MOKE approach remains at the forefront of magnetic nanostructure research performing high spatial and temporal resolution.

10.1. Imaging in SNOM

At the same time, as suggested by theoretical calculations, the size of the spin configuration peculiarities can be fairly small, and, consequently, conventional magnetization measurements fail to distinguish them from the surrounding magnetic structure. Moreover, observation of individual properties of the closely packed magnetic dots also demands for super-resolution. At this stage the SNOM microscopy—an optical technique with high spatial resolution—must be utilized. In spite of some technically removable difficulties in the extraction of the MO signal from the near-field images, this method allows a detailed investigation of the nanoscaled magnetization distribution.

To prove this statement, let us examine properties of the SNOM nonmagnetic and magnetic images. We consider scanning tunneling optical microscopy configuration of the SNOM (see Section 8). In this configuration a nanostructure is supposed to be located on the surface of a transparent substrate illuminated by linearly polarized light (wavelength $\lambda = 0.5\,\mu m$) at an incident angle beyond the limit of the total internal reflection (Figure 7.12). The light diffracted

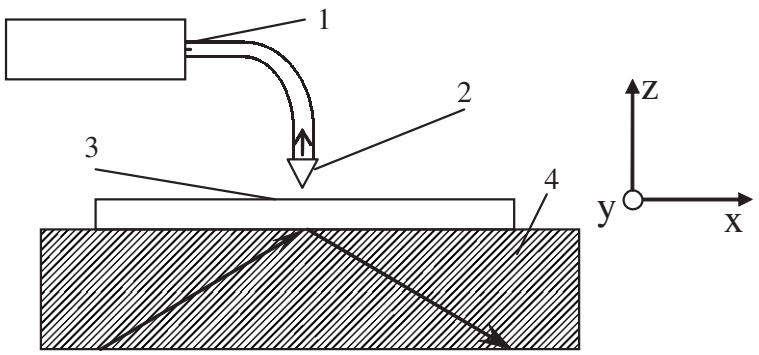

Figure 7.12. Schematic for scanning tunneling optical microscopy configuration. 1, detector; 2, optical probe; 3, sample; 4, substrate.

on the nanostructure is collected close to the sample surface by the tip of an optical fiber.

While performing calculations the following parameters were assumed. The refractive index of the semi-infinite substrate is $n = 1.5$, the incident angle is $\theta = 70°$ (angle of internal reflection for $n = 1.5$ equals to 42°). Polarization of the sample was supposed to be $P_{1i}^{(0)} = \varepsilon_0 \chi_{i,j} E_j^{(0)}$ (see Section 7), where the tensor of susceptibility is

$$\chi_{i,j} = \begin{pmatrix} n_1^2 - 1 & 0 & 0 \\ 0 & n_1^2 - 1 & 0 \\ 0 & 0 & n_1^2 - 1 \end{pmatrix} + \xi n_1^2 \begin{pmatrix} 0 & -im_z Q & im_y Q \\ im_z Q & 0 & -im_x Q \\ -im_y Q & im_x Q & 0 \end{pmatrix} \quad (21)$$

$m = (m_x, m_y, m_z) = M/M$, the unit magnetization vector. The first term in $\chi_{i,j}$ is a nonmagnetic part that can be called a crystalline one, and the second term in $\chi_{i,j}$ is a magnetic part (parameter $\xi = 0$ for nonmagnetic particle and $\xi \neq 0$ for the magnetic one).

For the images calculation the Green function technique described in Section 7 was utilized. Two main configuration of illumination were considered: s-polarization (incident polarization is perpendicular to the plain of incidence) and p-polarization (incident polarization is parallel to the plain of incidence). The electromagnetic field was calculated at a definite distance from the sample surface ("constant" height of scanning).

Simulations of the near-field images of nonmagnetic nanoparticles mounted on the surface of the dielectric substrate reveal one important feature (Figure 7.13): The plane of polarization rotates at the particle edges. Nonmagnetic rotation of polarization in near field is attributed to the fulfilling of boundary conditions at the boundaries between two conductors.

This fact should be taken into account in the interpretation of MO images, since MO observation exploits the property of a magnetized material to rotate the plane of wave polarization.

Bearing in mind that Q for magnetic materials is on the order of several hundredths, one can infer that a magnetic particle is difficult to be observed because of the unavoidable nongyrotropic rotation of the plane of polarization at its edges.

The MO contribution can be directly detected only at sites where the nonmagnetic contribution to the image approaches zero. Specifically, for a circular particle magnetized along the surface parallel to the plane of light incidence, the MO contribution becomes noticeable in crossed polarizers (the exponentially decaying background field is eliminated) at the edges parallel to the incident light (compare Figures 7.13 and 7.14).

Note that the nonmagnetic contribution is several hundred times higher than that of the MO component.

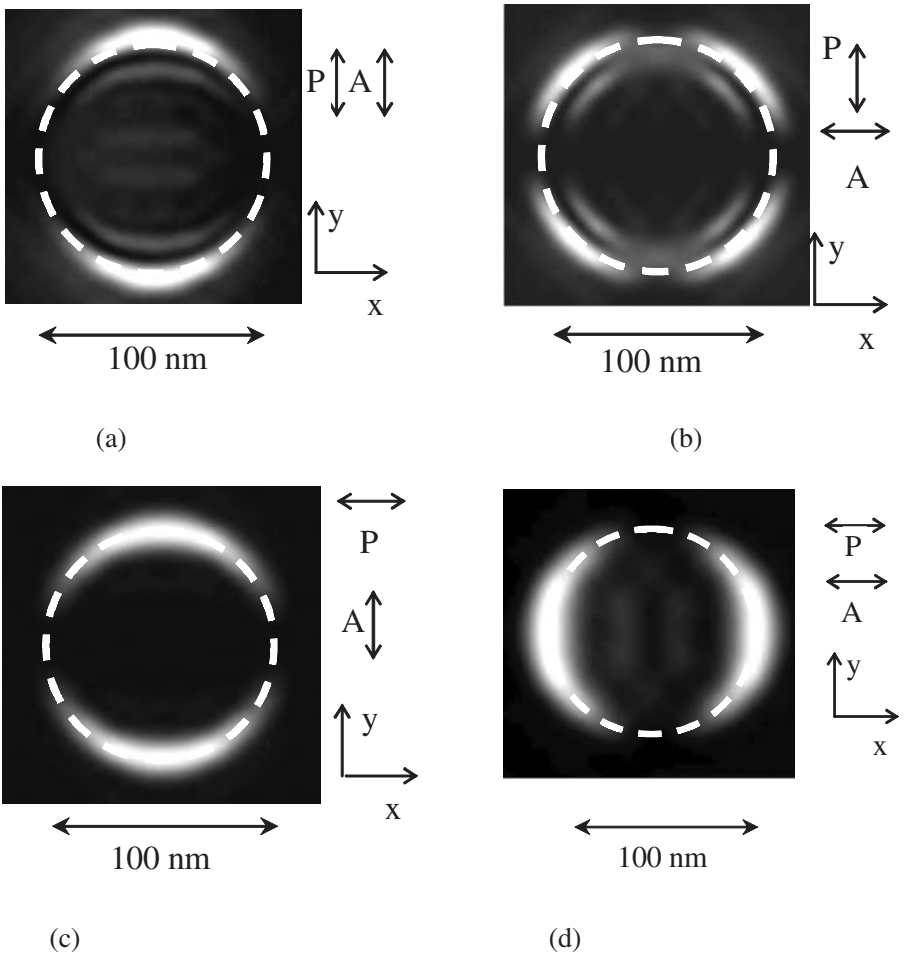

Figure 7.13. Simulated images of a nonmagnetic circle Ag particle (refractive index $n = 0.14 + i4.0$, diameter is 100 nm, thickness is 10 nm) under various illumination and observation conditions. The spatial resolution is 10 nm. A, analyzer; P, polarizer [46].

From the aforesaid, it follows that nonmagnetic inhomogeneities of nanoobjects (nanoparticle edges, lattice defects, etc.) make MO observations with SNOM difficult. Therefore, some special techniques are needed to extract the MO signal: modulation of the light polarization or working in the apertureless SNOM [68]. Another possibility is to detect the SNOM signal at the second optical harmonic that is generated on the surface of the sample [36, 40].

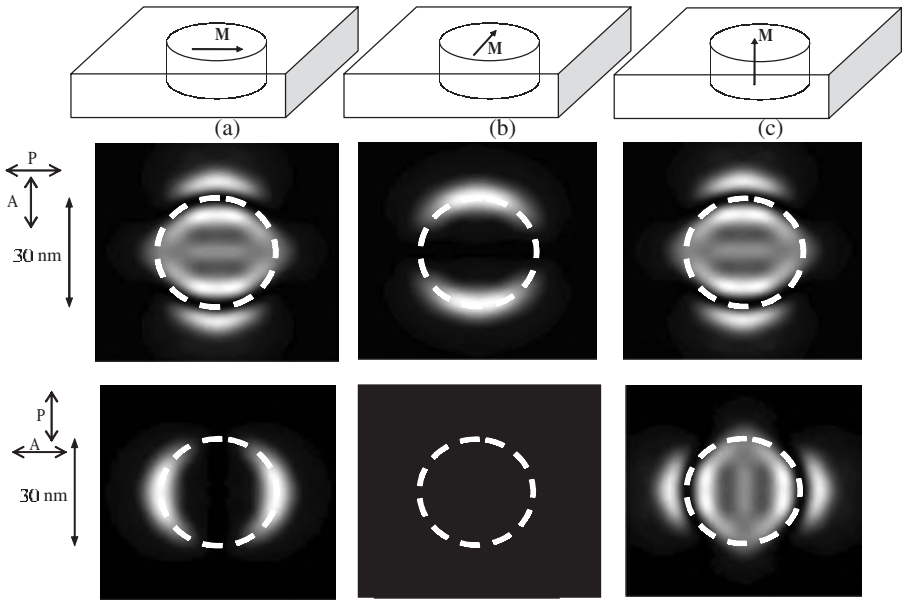

Figure 7.14. Simulated images of a 30-nm magnetic region embedded in a 10-nm-thick film under various illumination and observation conditions. The images of the nanoregion magnetized along the (**a**) *x*, (**b**) *y*, and (**c**) *z* axis are shown. The scan height is 11 nm, and the spatial resolution is 5 nm. A, analyzer; P, polarizer.

The other problem that arises during MO observation is that the SNOM resolution operating in transmission mode is limited not only by the size of the fiber-tip aperture but also by the thickness of the magnetic film [93–96].

The qualitative explanation of the decrease of resolution in SNOM gives Figure 7.15 [93]. Super-resolution beyond relay criterion is achievable by the presence of evanescent spatial harmonics in detected signal. With the increase of the sample's thickness, the contribution of these evanescent harmonics is reduced sharply: The contribution from the regions of the film that are located further than several hundred nanometers (for $\lambda \sim 0.5$ mkm) is almost entirely constituted by the far-field radiating components that are responsible for low-frequency space harmonics and low resolution. So we can conclude that a magnetic medium lying below this level does not contribute to the high resolution but only makes it worse. Consequently, the best results with transmission SNOM can be achieved only for thin (thickness is less than 300 nm).

Such a limitation for resolution does not exist for reflection measurements because this time only thin surface layers contribute to the image.

The other structure to be considered is a rectangular permalloy magnetic film of thickness 1 nm and size 200×500 nm. Simulation of the magnetization

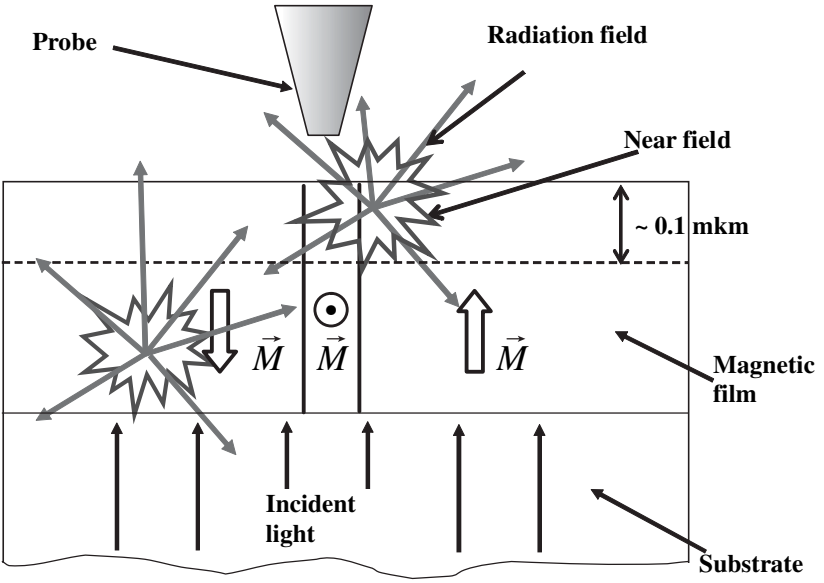

Figure 7.15. Radiation and nonradiation (near-field) fields arising in the magnetic film with the domain structure. Only near-field spatial harmonics radiated from the surface layer of several hundredths of a micrometer can reach the probe.

distribution in the sample with given geometrical and magnetic properties can be performed using the Landau–Lifshitz equation taking into account the full-scale magneto-dipole interaction [83] (Figure 7.16a).

In Figure 7.16b–e the calculated near-field images of the entire part of the sample for different orientation of cross-polarizers and plane of incidence are presented. Here again we consider the SNOM operating in the photon tunneling configuration. The brightest parts of the images correspond to the boundaries between the regions with uniform magnetization—that is, the domain walls. That is why it is possible to determine the shape and the size of magnetic nanometer-sized structures in the SNOM. For example, from Figure 7.16 one can estimate the width of the domain wall as 50 nm. This value is close to the "real" domain wall's width determined from the magnetization distribution in Figure 7.16a.

Finally we look at a SNOM image of the magnetic nanocontact region [83, 84, 97] (Figure 7.17a).

In this case the crystalline part of $\chi_{i,j}$ plays the main role in the image formation. This is because the banks of the nanocontact are not only magnetic edges but also crystalline ones. As we have already discussed, this brings about a very serious problem for the MO SNOM investigation of nanocontacts: In

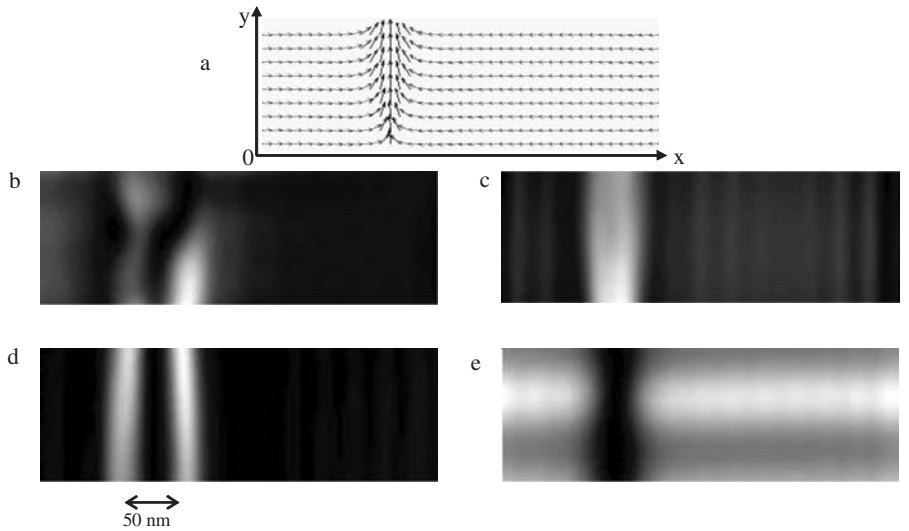

Figure 7.16. Magnetization distribution in rectangular permalloy magnetic film of thickness 1 nm (**a**) and simulated near-field images obtained in crossed polarizers for different orientations of incident polarization and plane of incidence: p-polarization, plane of light incidence is XZ plane (**b**); s-polarization, plane of light incidence is the *XZ* plane (**c**); p-polarization, plane of light incidence is *YZ* plane (**d**); s-polarization, plane of light incidence is the *YZ* plane. Height of scanning is 10 nm. Spatial resolution is about 15 nm. Intensities in (**c**) and (**e**) are two orders of magnitude smaller than that in (**b**) and (**d**).

near field the nonmagnetic rotation of polarization takes place on the crystalline edges of the structure, leading to extremely high intensities in the area of edges even during observation in cross-polarizers (Figure 7.17b). If crystalline contribution is subtracted from the image, then the magnetic structure becomes visible and one can observe the domain wall located at the center of the nanocontact. It is worth noting that the presence or absence of the domain wall influences substantially the transport properties of the nanocontact leading to the giant magnetoresistance effect [98].

10.2. Imaging in the ADFM

As we can see in Section 9, the ADFM technique is sensitive to the orientation of the nanoparticle magnetization vector and, being simple, may be useful and handy for studying the magnetization reversal. Combination of the ADFM technique with a high-speed photography setup presents a means for studying this

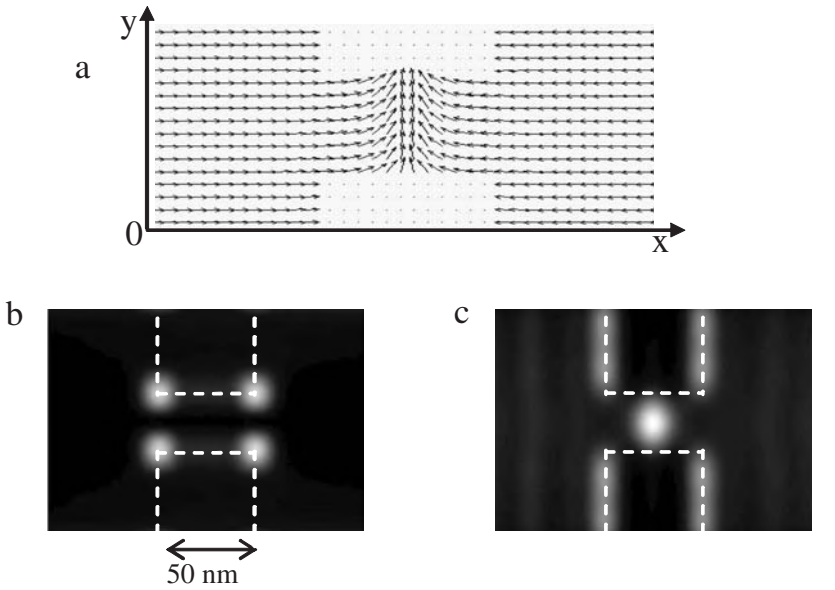

Figure 7.17. Magnetization distribution in magnetic nanocontact (**a**) and simulated near-field images obtained in crossed polarizers (s-polarization is incident, p-polarization is detected) for the case of light incidence parallel to the *XZ* plane: with (**b**) and without (**c**) taking into account the crystalline part of $\chi_{i,j}$ in equation (21). Height of scanning is 10 nm. Spatial resolution is about 15 nm.

process *in situ* with at least a nanosecond temporal resolution [99]—that is, during exposure to magnetic field pulses. We note that, according to theoretical and experimental estimations, the time of nanoparticle magnetization reversal is 10^{-12}–10^{-9} sec [100, 101].

The ADFM technique can also yield data on the magnetization state of an array of particles in the static case [21]. Indeed, by varying the azimuth angle of light incidence, one can construct the dependence of the array image intensity on the angle. The shape of the curves will depend on the scatter in the nanoparticle magnetization directions. Notwithstanding the fact that separate ADFM observation of nanoparticles is impossible at distances between particles shorter than $\lambda/2$, the change in the dark-field image intensity during the array magnetization reversal allows one to determine the average rate of remagnetization and to detect the presence of particles exhibiting dynamic properties differing from those of the majority of particles. Furthermore, the dependence of the image intensity on the azimuth angle of light incidence allows one to estimate the scatter in the particle magnetization directions in the static case.

References

1. K. O'Grady and H. Laidler, *J. Magn. Magn. Mater.* **200**, 616–633 (1999).
2. D. Weller, Plenary lecture at the Joint European Symposium on Magnetism, 28 August–1 September 2001, Grenoble, France (JEMS-2001).
3. L. D. Landau and E. M. Lifshitz, *Electrodynamics of Continuous Media*, Pergamon Press, New York, 1960.
4. P. Sheng, *Philos. Mag. B* **65**, 357–384 (1991).
5. W. T. Doyle and I. S. Jacobs, *Phys. Rev. B* **42**, 9319–9327 (1990).
6. F. Brouers, *J. Phys. C: Solid State Phys.* **19**, 7183–7193 (1986).
7. H. Ragossnig and A. Feltz, *J. Eur. Ceramic Soc.* **18**, 429–444 (1998).
8. M. Wu, H. Zhang, Xi Yao, and L. Zhang, *J. Phys. D: Appl. Phys.* **34**, 889–895 (2001).
9. L. Tsang, J. A. Kong, and R. T. Shin, *Theory of Microwave Remote Sensing*, John Wiley & Sons, New York, 1985, pp. 425–475.
10. Y. Rao, C. P. Wong, and J. Qu, *IEEE Trans. CPMT* **23**, 680 (2000).
11. D. Stroud, *Superlattices Microstruct.* **23**, 567 (1998).
12. H. C. Van de Hulst, *Light Scattering by Small Particles*, Dover, New York, 1969 or 1981.
13. M. Lax, *Rev. Mod. Phys.* **23**, 287 (1951).
14. M. Kerker, *The Scattering of Light and Other Electromagnetic Radiation*, Academic, New York, 1969.
15. J. C. Maxwell Garnett, *Philos. Trans. R. Soc. A* **203**, 385 (1904).
16. R. Ruppin. *Opt. Commun.* **182**, 273–279 (2000).
17. D. M. Wood and N. W. Ashcroft, *Phys. Rev. B* **25**(10), 6255 (1982).
18. H. Ragossnig and A. Feltz, *J. Eur. Ceram. Soc.* **18**, 429–444 (1998).
19. D. A. G. Bruggeman, I. *Ann. Phys. Leipzig* **24**, 636–664 (1935).
20. R. Pelster and U. Simon, *Colloid Polym. Sci.* **277**, 2 (1999).
21. V. I. Belotelov, A. K. Zvezdin, V. A. Kotov, et al., *Phys. Solid State* **45**, 1957 (2003).
22. N. F. Kubrakov, A. K. Zvezdin, K. A. Zvezdin, et al., *JETP* **87**, 600 (1998).
23. R. Atkinson, N. F. Kubrakov, A. K. Zvezdin, and K. A. Zvezdin. *J. Magn. Magn. Mater.* **156**, 169 (1996).
24. R. Q. Hood and L. M. Falikov. *Phys. Rev.* **B46**, 8287 (1992).
25. D. Bozec, V. G. Kravets, J. A. D. Matthew, and S. M. Thompson, *J. Appl. Phys.* **91**, 8795 (2002).
26. A. K. Zvezdin, V. A. Kotov, *Modern Magneto-Optics and Magneto-Optical Materials*, IOP Publishing, Philadelphia (1997), 363 pages.
27. R. V. Pisarev, *Physics of Magnetic Dielectrics*, Moscow, Nauka (1974).
28. B. E. Argile and E. Terrenzio, *J. Appl. Phys.* **55**, 2569–2579 (1984).

29. G. S. Krinchik, *Physics of Magnetic Phenomena*, Moscow State Universty Press, Moscow (1985).
30. G. S. Krinchik and E. E. Chepurova, *Proceedings ICM-73*, Moscow State University Press, Moscow (1973), p. 139.
31. J. Shoenes, *J. Magn. Soc. Jpn. Suppl.* **11**, 99 (1987).
32. P. Guyot-Sionnest and Y. R. Shen, *Phys. Rev. B* **35**, 4420 (1987).
33. U. Pustogowa, W. Hubner, and K. H. Benneman, *Phys. Rev. B* **48**, 8607 (1993).
34. Ru-Pi Pan, P. D. Wel, and Y. R. Shen, *Phys. Rev. B* **39**, 1229 (1989).
35. A. K. Zvezdin and N. F. Kubrakov, *JETP* **116**, 141 (1999).
36. V. I. Belotelov, A. P. Pyatakov, S. A. Eremin et al., *Physics of the Solid State* **42**, 1873 (2000).
37. U. Pustogowa, W. Hubner, and K. H. Benneman, *Phys. Rev. B* **49**, 1031 (1994).
38. O. A. Aktsipetrov, E. A. Gan'shina, V. S. Guschin et al., *J. Magn. Magn. Mater.* **196**, 80 (1999).
39. B. Koopmans, M. J. K. Koerkamp, and T. Rasing, *Phys. Rev. Lett.* **74**, 3692 (1995).
40. V. I. Belotelov, A. P. Pyatakov, G. G. Musaev et al., *Opt. Spectrosc.* **91**, 626 (2001).
41. O. A. Aktsipetrov, V. A. Aleshkevich, A. V. Melnikov et al., *J. Magn. Magn. Mater.* **165**, 421 (1997).
42. T. M. Crawford, C. T. Rogers, and T. J. Silva et al., *J. Appl. Phys.* **81**, 354 (1997).
43. A. A. Maradudin and D. L. Mills, *Phys. Rev. B* **11**, 1392 (1975).
44. D. L. Mills and A. A. Maradudin, *Phys. Rev. B* **12**, 2943 (1975).
45. V. A. Kosobukin, *Phys. Solid State* **35**, 884 (1993).
46. V. I. Belotelov, A. P. Pyatakov, A. K. Zvezdin, et al., *Tech. Phys.* **48**, 1–6 (2003).
47. O. J. F. Martin, C. Girard, and A. Dereux, *Phys. Rev. Lett.* **74**, 526 (1995).
48. V. A. Kosobukin, *JTP* **43**, 824 (1998).
49. M. Paulus, P. Gay-Balmaz, and O. J. F. Martin, *Phys. Rev. E* **62**, 5797 (2000).
50. Y. Martin and H. K. Wickramasinghe, *Appl. Phys. Lett.* **50**, 1455 (1987).
51. S. Hosaka, A. Kikukawa, and Y. Honda, *Appl. Phys. Lett.* **65**, 3407 (1994).
52. I. V. Yaminskioe and A. M. Tishin, *Usp. Khim.* **68**, 187 (1999).
53. D. Courjon and C. Bainier, *Rep. Prog. Phys.* **57**, 989 (1994).
54. D. W. Pohl, *Thin Solid Films* **264**, 250–254 (1995).
55. M. Ohtsu *Near Field Nano/Atom Optics and Technology*, Springer, Tokyo (1998), 297 pages.
56. G. S. Zhdanov, M. N. Libenson, and G. Marcinovskiy, *Phys. Uspekhi* **41**, 719 (1998).
57. E. Betzig and J. K. Trautman, *Science* **257**,189–195 (1992).
58. M. A. Paesler and P. J. Moyer, *Near-Field Optics Theory, Instrumentation and Applications*, John Wiley & Sons, New York (1996).

59. D. Courjon, J. M. Vigoureux, M. Spajer et al., *Appl. Opt.* **29**, 3734 (1990).
60. K. D. Weston, J. A. DeAro, and S. K. Buratto, *Rev. Sci. Inst.* **67**, 2924–2929 (1996).
61. E. Betzig, P. L. Finn, and J. S. Weiner, *Appl. Phys. Lett.* **60**, 2484–2486 (1992).
62. E. Betzig, J. K. Trautman, R. Wolfe et al., *Appl. Phys. Lett.* **61**, 142 (1992).
63. U. Hartmann, *J. Magn. Magn. Mater.* **157/158**, 545 (1996).
64. E. Betzig, J. K. Trautman, J. S. Weiner et al., *Appl. Opt.* **31**, 4563 (1992).
65. T. J. Silva, S. Schultz, *Rev. Sci. Instrum.* **67**, 715 (1996).
66. P. Fumagalli, A. Rosenberger, G. Eggers et al., *Appl. Phys. Lett.* **72**, 2803 (1998).
67. G. Eggers, A. Rosenberger, N. Held, et al., *Ultramicroscopy* **71**, 249 (1998).
68. H. Wioland, O. Bergossi, S. Hudlet, et al., *Eur. Phys. J. AP* **5**, 289 (1999).
69. T. Lacoste, T. Huser, and H. Heizelmann, *Z. Phys. B.* **104**, 183 (1997).
70. A. A. Ejov, A. S. Logginov, D. A. Muzychenko, A. V. Nikolaev, and V. I. Panov. *Poverkhn. Yavieniya Polim.* **11**, 56 (2000).
71. M. Nieto-Vesperinas and J. C. Dainty, *Scattering in Volumes and Surfaces*, Madrid (1990).
72. R. W. Ditchburn, *Light*, 2nd ed., Blackie, London (1963).
73. B. Kuhlow and M. Lambeck, *Physica B & C (Amsterdam)* **80**, 374 (1975).
74. A. Thiaville and F. Boileau, J. Miltat et al., *J. Appl. Phys.* **63**, 3153 (1988).
75. A. Thiaville and J. Miltat, *IEEE Trans. Magn.* **26**, 1530 (1990).
76. A. S. Logginov, A. V. Nikolaev, and V. V. Dobrovitski, *IEEE Trans. Magn.* **29**, 2590 (1993).
77. A. S. Logginov, A. V. Nikolaev, and V. N. Onishchuk, in *Proceedings of Conference on Physics of Condensed States*, Vol. 2, Sterlitamak. Gos. Pedagog. Institute, Sterlitamak (1997), p. 50.
78. V. I. Belotelov, A. S. Logginov, and A. V. Nikolaev, *Radiotekh. Élektron. (Moscow)* **46**, 870 (2001).
79. A. P. Malozemoff and J. C. Slonczewski, *Magnetic Domain Walls in Bubble Materials*, Academic, New York (1979).
80. A. Hubert and R. Schafer, *Magnetic Domains*, Springer, Berlin (1998).
81. T. Shinjo, T. Okuno, R. Hassdorf et al., *Science* **289**, 930–932 (2000).
82. J. Sasaki and F. Matsubara, *J. Phys. Soc. Jpn.* **66**, 2138 (1997).
83. K. A. Zvezdin, *Solid State Phys.* **42**, 1 (2000).
84. A. K. Zvezdin and K. A. Zvezdin. *JETP Lett.* **95**, 762–767 (2002).
85. D. A. Allwood, G. Xiong, M. D. Cooke et al., *J. Phys. D: Appl. Phys.* **36**, 2175–2182 (2003).
86. R. P. Cowburn, *Phys. Rev. B* **65**, 092409 (2002).
87. R. P. Cowburn, D. K. Koltsov, A. O. Adeyeye et al., *Phys. Rev. Lett.* **83**, 1042 (1999).
88. T. Aign, P. Meyer, S. Lemerle et al., *Phys. Rev. Lett.* **81**, 5656 (1998).

89. V. I. Belotelov, A. S. Logginov, and A. V. Nikolaev, *Physics of the Solid State*. **45**, 519 (2003).
90. D. P. E. Dickson, N. M. K. Reid, and C. A. Hunt, *J. Magn. Magn. Mater.* **125**, 345 (1994).
91. W. Wernsdorfer, E. Bonet Orozco, and K. Hasselbach et al., *Phys. Rev. Lett.* **78**, 1791 (1997).
92. J. P. Jamet, J. Ferre, P. Meyer et al., *IEEE Trans. Magn.* **37**, 2120 (2001).
93. V. I. Belotelov, A. S. Logginov, A. P. Pyatakov et al., *Technical Digest IQEC 2002*, Moscow, June, p. 368.
94. A. A. Ezhov, A. S. Logginov, D. A. Muzychenko, A. V. Nikolaev, and V. I. Panov, *Phys. Metals Metallogr.* (Supplementary Issue), **92**(1), 277 (2001).
95. P. Bertrand, L. Colin, V. I. Safarov. *J. Appl. Phys.* **83**, 6834 (1998).
96. A. A. Ejov, A. S. Logginov, D. A. Muzychenko, A. V. Nikolaev, and V. I. Panov, *Poverchn. Yavieniya Polim.* **11**, 56 (2000).
97. A. K. Zvezdin and A. F. Popkov, *JETP Lett.* **71**, 209 (2000).
98. N. Garsia, M. Munoz, and Y. W. Zhao, *Phys. Rev. Lett.* **82**, 2923 (1999).
99. L. P. Ivanov, A. S. Logginov, and G. A. Nepokooechitskiy, *Sov. Phys. JETP* **57**, 583 (1983).
100. D. P. E. Dickson, N. M. K. Reid, and C. A. Hunt, *J. Magn. Magn. Mater.* **125**, 345 (1994).
101. W. Wernsdorfer, E. Bonet Orozco, K. Hasselbach et al., *Phys. Rev. Lett.* **78**, 1791 (1997).